



Article

Experimental Study on the Butterfly Shape of the Plastic Zone around a Hole near Rock Failure

Wenlong Zhang ¹ , Jiajia Yu ², Jianju Ren ^{3,*}, Chen Li ⁴ and Ji Ma ⁵

¹ School of Civil Engineering and Architecture, Qingdao Huanghai University, Qingdao 266427, China; wenlong0523@163.com

² Zhejiang Qinhe Environmental Construction Co., Ltd., Jiaxing 314300, China; 18678838665@163.com

³ School of Resource Engineering, Xi'an University of Architecture and Technology, Xi'an 710055, China

⁴ CCTEG Wuhan Engineering Company & Research Institute Co., Ltd., Wuhan 430064, China; 13120008810@163.com

⁵ College of Safety Science and Engineering, Henan Polytechnic University, Jiaozuo 454003, China; showsma@hpu.edu.cn

* Correspondence: rjj18049300680@xauat.edu.cn

Abstract: The precursor of rock failure around a hole has always been one of the research hotspots in the field of rock mechanics, and the distribution of the plastic zone is often adopted to reflect the location and form of rock failure. The shape of the plastic zone around a hole before rock failure can guide the mechanism of and early warning methods for geotechnical engineering disasters, while previous theoretical research and numerical simulation results show that the shape of the plastic zone around the hole is butterfly shaped under specific stress, which is referred to as butterfly failure theory. Studies also indicate that the butterfly shape of the plastic zone around a hole is considered to be the main cause of many disasters, which signifies the importance of studying the morphology of the plastic zone near rock failure. Therefore, this study is committed to finding the specific shape of the plastic zone near rock failure through relatively accurate and a high number of AE event location results, and the final experimental results show that the plastic zone around the hole is basically a butterfly shape near rock failure. This study verifies the correctness of the butterfly failure theory and provides an important reference for the study of geotechnical engineering disaster mechanisms and monitoring methods. The fact that the plastic zone in the early stage of rock failure in this study tends to be butterfly shaped preliminarily indicates the fractal law of rock failure. In the moment before rock failure, the distribution of AE events is more regular, which leads to large-scale collapse type failure.

Keywords: rock failure; plastic zone; butterfly shape; around hole; source scanning algorithm



Citation: Zhang, W.; Yu, J.; Ren, J.; Li, C.; Ma, J. Experimental Study on the Butterfly Shape of the Plastic Zone around a Hole near Rock Failure.

Fractal Fract. **2024**, *8*, 215. <https://doi.org/10.3390/fractalfract8040215>

Academic Editors: Lihai Tan, Xiaohan Yang and Zine El Abiddine Fellah

Received: 3 March 2024

Revised: 1 April 2024

Accepted: 4 April 2024

Published: 7 April 2024



Copyright: © 2024 by the authors. Licensee MDPI, Basel, Switzerland. This article is an open access article distributed under the terms and conditions of the Creative Commons Attribution (CC BY) license (<https://creativecommons.org/licenses/by/4.0/>).

1. Introduction

The mechanism, form, monitoring, and early warning methods of rock failure have always been one of the key problems in rock mechanics research. The sudden destruction of rock often causes many geotechnical disasters, such as roof fall [1], rock burst [2,3], collapse [4], earthquake [5], and so on, which poses a great security threat to human production activities [6]. Rock failure is a macro phenomenon, which is caused by the continuous generation and accumulation of plastic zones under a principal stress field [7]. The failure of rock is mainly divided into three forms: compressive failure, tensile failure, and shear failure, which correspond to compressive strength, tensile strength, and shear strength, respectively. The theory of rock failure mainly includes strength theory (like Coulomb–Mohr, von Mises, and Tresca), energy theory, rock burst tendency theory, instability theory, etc. According to the frequently used Coulomb–Mohr theory, rocks are destroyed either by tension or shear. Regardless of the form of damage or failure, plastic zones should normally occur. The plastic zone is the state when the applied force reaches

the yield strength, and if the rock continues to bear greater force, it will reach the peak strength and then produce failure [8].

Theoretically, rock failure will occur when the imposed corresponding force of rock exceeds one of the compressive strength, tensile strength, and shear strength values. Of the three strengths, the compressive strength is usually the highest and the tensile strength is usually the lowest. In the field of engineering, rock is often damaged by high compressive stress [9,10], which is considered to be dangerous. Rock compressive failure can be divided into six stages: the elastic deformation stage, the linear elastic deformation stage, the plastic deformation stage, the pre-peak stage, the softening stage, and the residual strength stage. This process is accompanied by crack compaction, elastic deformation, new crack generation, and large-scale failure [11]. Of course, in addition to the influence of external forces, the properties of rocks themselves and the external environment also have certain influences, such as the distribution of cracks or weak inclusions [12] and temperature and humidity [13].

The shape and distribution characteristics of the plastic zone around a hole before failure are worth studying [14,15], and they are directly related to the disclosure of disaster mechanisms and methods of early warning [16]. In studies from recent years, the shape of the plastic zone around a hole can be roughly divided into a circle, ellipse, or butterfly (X shape) under different mechanical states obtained through theoretical calculation [17,18] and numerical simulation [19,20], and these features are called butterfly failure theory [21]. Under the action of a uniform stress field (the principal stresses in three directions are the same), the shape of the plastic zone around the hole is circular [22]. When the ratio of the maximum principal stress to the minimum principal stress is small (like 1.5), the shape of the plastic zone around the hole is roughly elliptical [23], whereas when the ratio of the maximum principal stress to the minimum principal stress reaches more than about 2.5, the shape of the plastic zone around the hole changes to a butterfly shape [24], which is considered extremely dangerous. Butterfly failure theory has been successfully used to reveal the mechanisms of many dynamic disasters such as rock burst [25,26], roof fall [27], earthquake [28,29], fault formation [30], coal and gas outburst [31], and so on. But it should be pointed out that research on the shape of the plastic zone around a hole only involves the use of theoretical research and numerical simulation methods and it has not been perfectly verified at the laboratory and field scales.

While the plastic zone forms, the rock will produce a lot of additional information, such as acoustic emission (AE) [32,33], electromagnetic [34], sound [35], and so on, which are often used as monitor indicators to reflect material failure [36–38]. Among this information, capturing AE signals to reflect the location of rock fracture is the most commonly used method in laboratory tests [39]. The indicators used to characterize AE events usually include amplitude (voltage value) [40], particle velocity [41], event duration [42], dominant frequency [43], occurrence location [44], fractal dimension [45], etc., and these indicators have been confirmed to be effective for rock failure monitoring. The location of AE events can better reflect the central occurrence position of the fracture [46], but the accuracy of positioning is usually very dependent on algorithms [47]. The commonly used algorithms mainly include cluster analysis [48], machine learning [49], arrival time difference location [50], the source scanning algorithm (SSA) [51,52], and so on. The arrival time difference location method usually depends on the accurate arrival time point pickup, while the SSA does not depend on the take-off point and finds the optimal solution through the brightness function [53].

The main purpose of this study was to accurately determine the occurrence location of AE events in a rock sample with a central hole. Therefore, large-scale rock samples with a central hole, a high sampling frequency AE instrument, and an appropriate algorithm were applied to calculate the location results. In this study, the shape of the plastic zone around a hole can be fed back by AE events to reflect the characteristics of rock before failure, which can lay a foundation for failure mechanisms and early warning methods for engineering

disasters. At the same time, the correctness of butterfly failure theory and butterfly plastic zone shape under specific stress can be verified at the laboratory scale.

2. Method

The purpose of this study was to determine the distribution of AE events of a relatively large sample with a central hole under uniaxial compression, so as to reveal the plastic zone shape of rock near failure (it should be pointed out that the numerical simulation results show that the butterfly plastic zone still appeared before failure under uniaxial compression; therefore, only vertical uniaxial loading was applied in this study for the convenience of the experiment). The experimental devices used mainly included a universal tester, a tester control system, an AE acquisition instrument, sensors, a computer display, the rock sample, and so on, as shown in Figure 1 and Table 1 (model and other parameters). The universal tester can provide a maximum vertical pressure of 5000 kN and cooperate with the control system to achieve accurate displacement loading. The model of the AE acquisition instrument was DS5-16, which can realize synchronous data acquisition of 2~16 channels; the sampling frequency was 6 MHz when 8 channels were used, and the continuous data passing rate was 113 MB/s. The receiving frequency of the sensor was 50~400 kHz and the center receiving frequency was 150 kHz. The computer display and supporting software were used to collect and show the collected data.



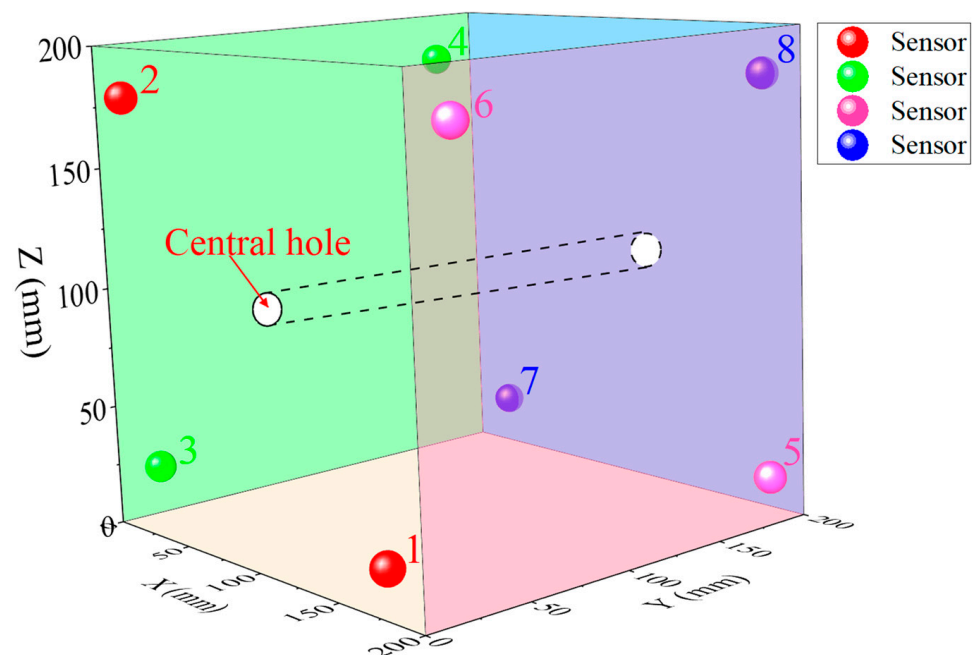
Figure 1. General layout of the experimental device.

The rock sample was a purchased finished product with a size of $200 \times 200 \times 200$ mm (a small hole with a diameter of 20 mm was set in the center to represent a roadway, tunnel, etc.), which was taken from the roof rock stratum of a rock burst coal mine. The material of the rock sample was sandstone. After being taken in blocks from the top plate, it was cut in the laboratory, polished, and finally drilled to form a finished product. Observed through a magnifying glass, the sandstone component of the sample was relatively fine and belonged to fine-grained sandstone. Due to its high compressive strength, the uniaxial compressive strength was around 70 MPa according to the manufacturer's test results. The manufacturer also evaluated the rock burst tendency of the sandstone, and the results showed weak burst properties.

Table 1. Parameters of the main experimental device.

Device	Model	Other Main Parameters
Universal tester	YAW-5000	Vertical pressure: 5000 kN; Piston stroke: 0–1500 mm; Constant velocity stress control range: 1–10 N/m
AE acquisition instrument	DS5-16	Data acquisition: 2~16 channels Sampling frequency: 6 MHz when 8 channels were used
AE sensors	VS150	Receiving frequency: 50~400 kHz; Center receiving frequency: 150 kHz

The AE sensor arrangement of the rock sample is displayed in Figure 2; a total of eight sensors were set to ensure sufficient data acquisition. All eight sensors were installed directly on four sides of the rock sample according to the vertical loading method, and two sensors were set on each side. The two sensors on each side were installed on two opposite corners and staggered with the opposite side in order to improve the rationality of the network. The (x, y, z) coordinates of sensors 1#~8# were (0.18, 0, 0.02) m, (0.02, 0, 0.18) m, (0, 0.02, 0.02) m, (0, 0.18, 0.18) m, (0.2, 0.18, 0.02) m, (0.2, 0.02, 0.18) m, (0.02, 0.2, 0.02) m, and (0.18, 0.2, 0.18) m, respectively. Before experimental loading, the sensors and the rock sample were bonded together by high-strength glue to ensure the integrity of the collection.

**Figure 2.** AE sensor arrangement of the rock sample.

Through the above relatively large-size sample and high sampling frequency AE signal acquisition system, the high-precision acquisition of AE events could be ensured, and the basis for the accurate positioning of AE events could be provided. The accurate location of AE events could reflect the failure time and location of the rock sample, which could provide real basic data to accurately reflect the shape of the plastic zone under the specific stress state in this study. The research results may provide a new idea for rock failure precursors, geotechnical engineering disaster occurrence mechanisms, and disaster monitoring and early warning methods.

3. Results

Before uniaxial loading and AE signal acquisition, the wave velocity of the sample was first tested, and the average result was 1989 m/s, which was used for subsequent AE event

location. After the experiment, the loading stress–strain curve and detailed AE signal data were obtained. The stress–strain curve of the experimental rock sample obtained is shown in Figure 3; the results indicated that the sample showed obvious elastic characteristics, which may be related to the rock burst tendency of the medium. The peak intensity of the sample was 69.691 MPa, which occurred at 1993 s (taking the time of initial loading as 0 s), and the sample showed a sudden failure phenomenon after the peak intensity. The results of the stress–strain curve showed that there was basically no obvious yield strength point for the sample. After the elastic stage, it directly reached the strength limit (peak intensity) and then presented sudden instantaneous failure. It was appropriate to accurately locate the AE event of this kind of rock with a rock burst tendency to reflect the shape of the plastic zone before failure.

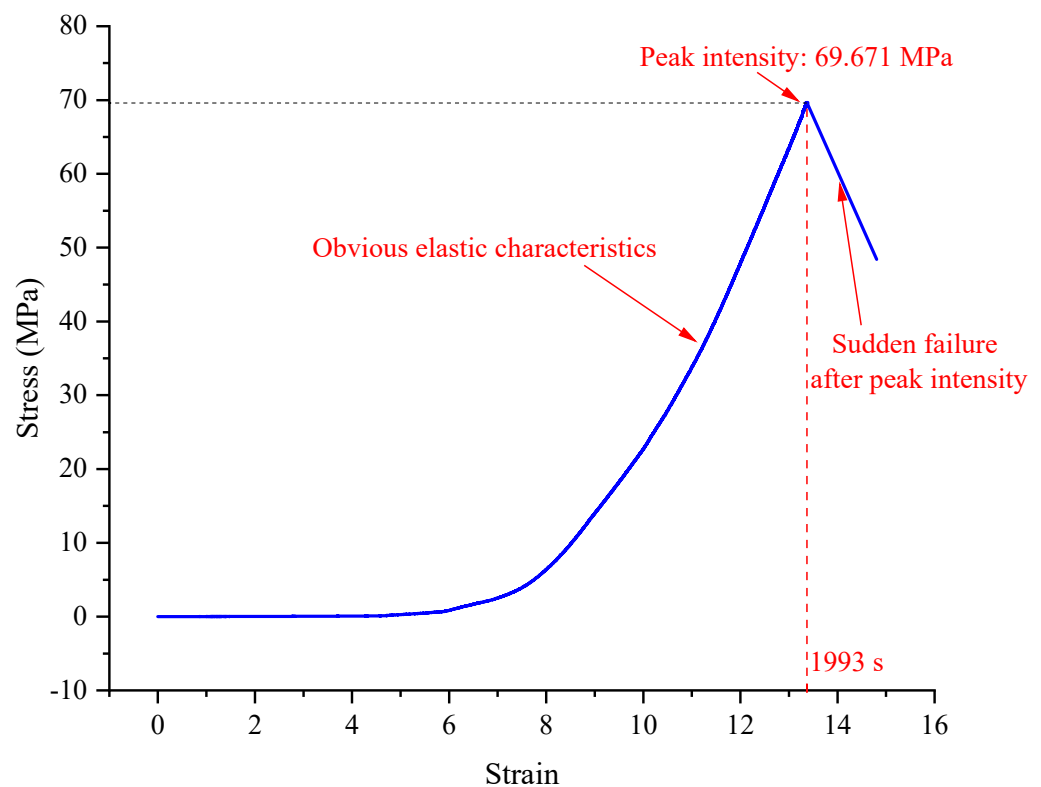


Figure 3. Stress–strain curve of the experimental rock sample.

Figure 4 shows the respective change diagram of signal energy during the entire loading process, and the loading process could be divided into four stages according to the loading stress curve and energy relationship: the early minor failure stage, the intermediate elastic stability failure stage, the late unstable failure stage, and the final large-scale failure stage. The corresponding time periods of the four stages were 0~1100 s, 1100~1900 s, 1990~1990 s, and 1990~1995 s, respectively, and the corresponding stress ranges were <3 MPa, 3~58 MPa, 58~68 MPa, and 68~69 MPa, respectively. During the first stage, the energy was generally less than 2500 mV*ms, and there were two larger energy bands in the range of 90~100 s and 370~400 s. In the second stage, the energy was even lower than that in the first stage, indicating that the damage in the elastic stage was relatively small, which was the same as the result in a previous study [54]. In the third stage, the energy became abnormally high and unstable, and the energy was the highest in the fourth stage, which led to the large-scale failure of the sample.

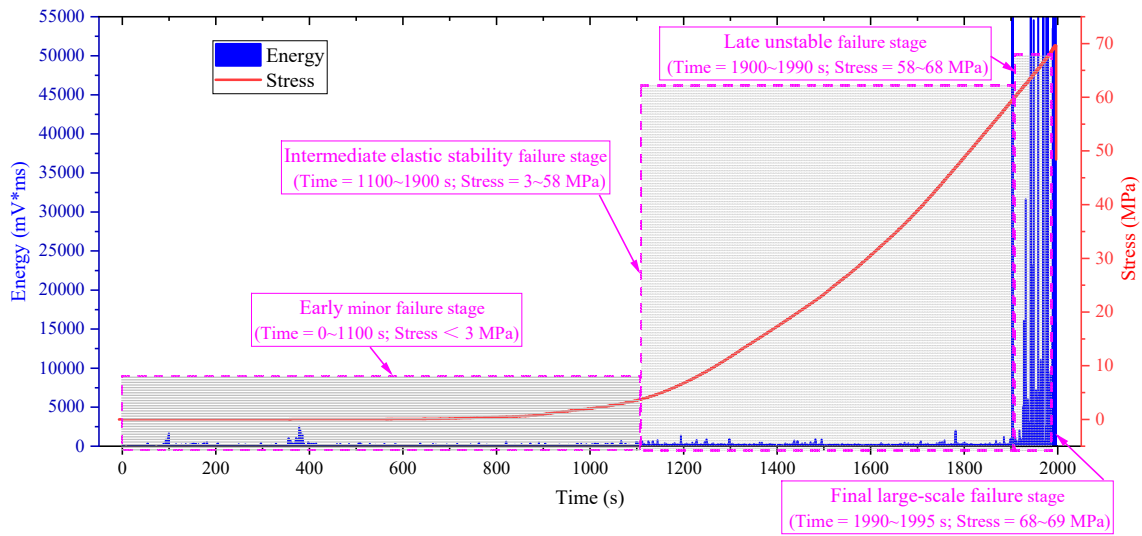


Figure 4. Energy stage during the entire experimental process.

The amplitude changes of the eight sensors during the experiment are shown in Figure 5. It can be seen from the figure that there was mainly four AE event regions (I, II, III, and IV), which occurred at 95~100 s, 370~380 s, 1050~1550 s, and 1900~1995 s, respectively. Region I and II usually caused eight channels to generate AE waveforms. Region III was located in the intermediate elastic stability failure stage, which only caused some channels to generate AE waveforms in most cases. The early part of region IV also caused some channels to generate AE waveforms, but the later part of region IV usually caused all eight channels to generate AE waveforms. After checking the basic waveform, the AE event characteristics in regions I, II, and III were obvious, and the take-off points were clear; one case event waveform is shown in Figure 6 (occurring within 99 s). The case event waveform showed that the arrival time of the waveforms were clear, and the amplitude differences of the eight sensors were small, indicating that the distances between the event location and the sensors were similar, and the preliminary conclusion was that the event may have occurred around the central hole.

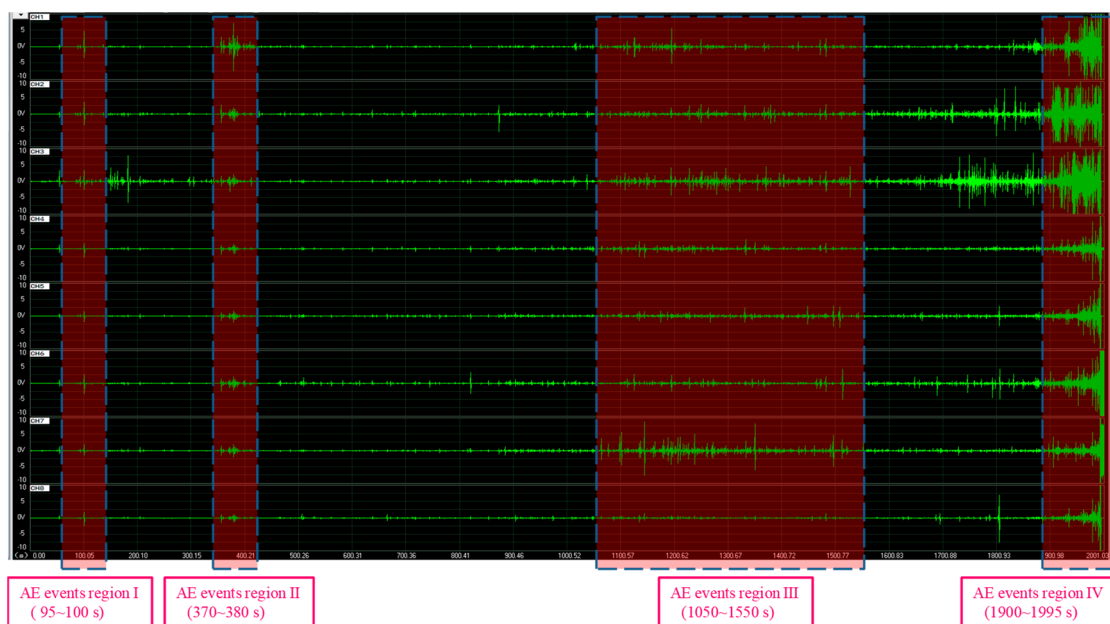


Figure 5. AE event regions during the experimental process.

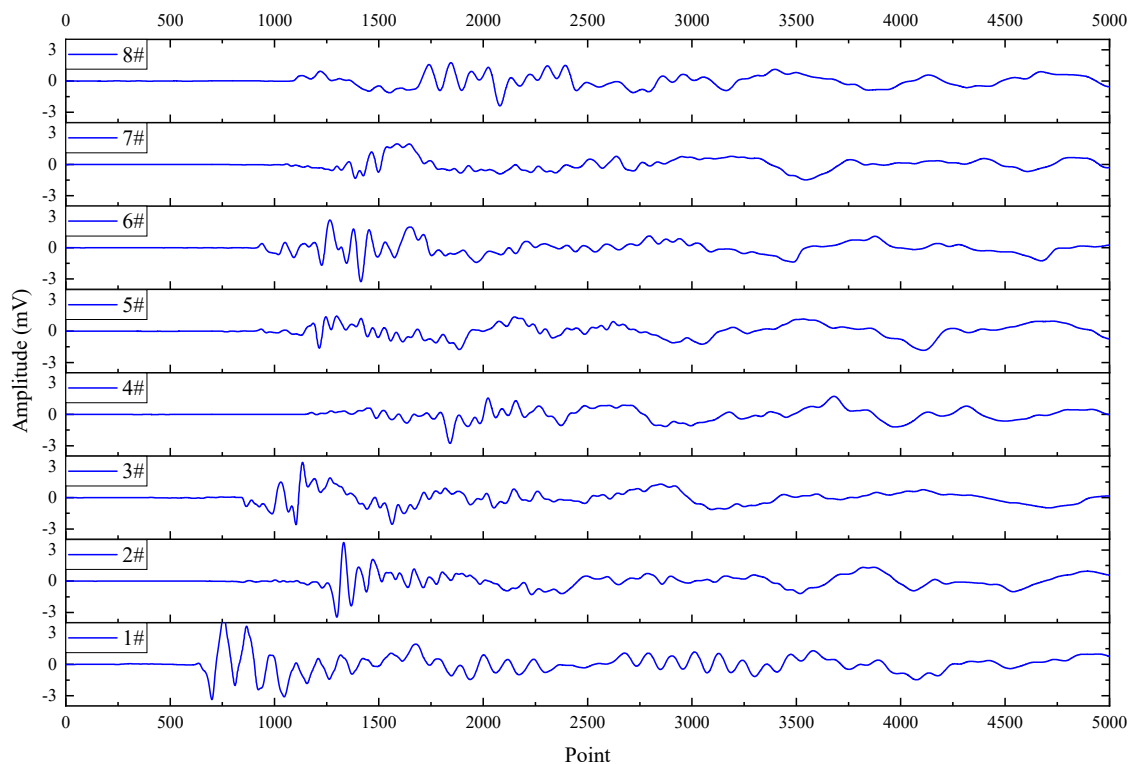


Figure 6. Case event waveforms occurring within 99 s.

From the results in Figure 6, the waveform characteristics obtained by the eight channels were consistent with the AE event characteristics, the arrival time was clear, and the amplitude conformed to the conventional law, which showed that more accurate actual positioning points could be obtained by using the ordinary algorithm. However, the basic waveform of the later events (occurring in 1992 s) was very different from that of the early events, and the case event waveforms are shown in Figure 7. The take-off points of the latter case waveforms were not all clear, and the arrival times of eight channels could not be extracted normally, which meant that it was not possible to determine the location of events unable by using the common arrival time difference method. It is also worth noting that the amplitude of the case waveforms in Figure 7 were particularly large, and the waveforms fluctuated and jumped violently, indicating that the fracture size of the sample was large, which resulted in the waveforms overlapping and showing insensitivity.

Some basic waveforms, especially those occurring during the large-scale destruction period in the later stage, could not accurately pick up the take-off point, and the conventional location algorithm that depended on the take-off point was not able to work; therefore the SSA independent of the take-off point (depends on luminance function) was used for the event location in this study. A scatter plot and heat map of the AE event distribution during the four typical periods (90~100 s, 370~380 s, 1060~1070 s, and 1990~1995 s) are denoted in Figure 8; the results show that the number of AE events showed an overall growth trend, which were 187 (lasting for 10 s), 1577 (lasting for 10 s), 4800 (lasting for 10 s), and 4705 (lasting for 5 s), as shown in Table 2. From the positioning results, the initial failure range was small, and the later failure range was large, with it reaching the boundary of the sample. From the perspective of the failure shape, there was no obvious law of failure during 90~100 s, and the results in the heat map shown that there were more event points around the central hole. The failure shape of 370~380 s was similar to an ellipse, while the failure shape of 1160~1170 s was close to a butterfly (X shape), and the failure mode of 1990~1995 s was most close to a butterfly shape.

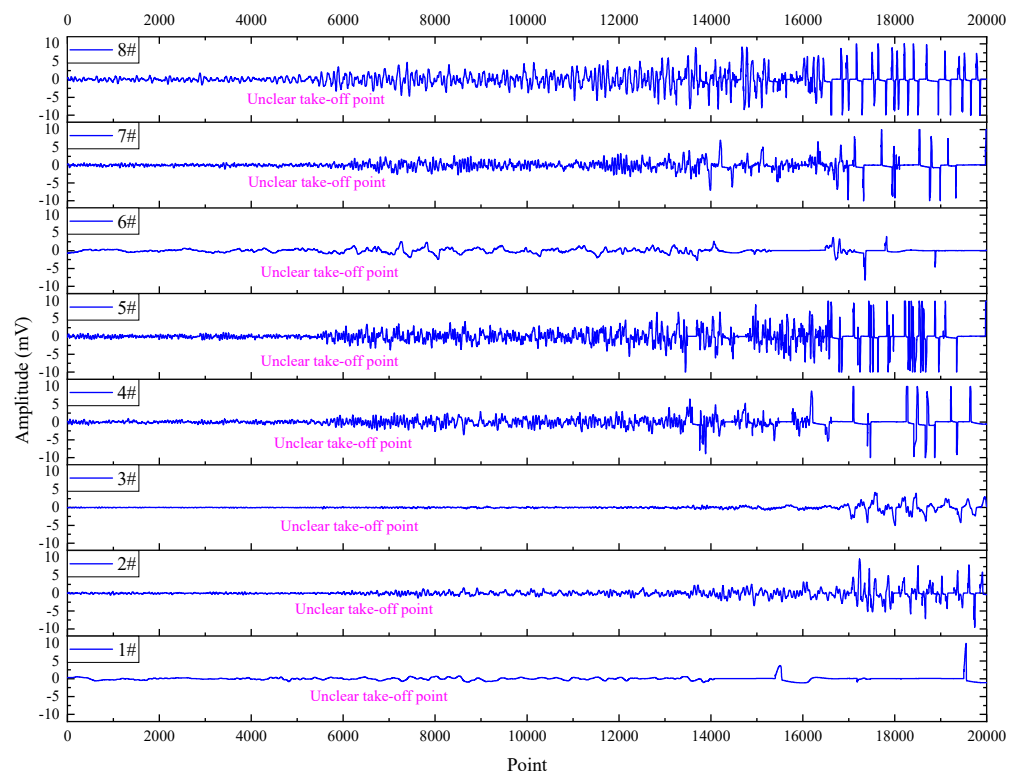


Figure 7. Case event waveforms occurring in 1992 s.

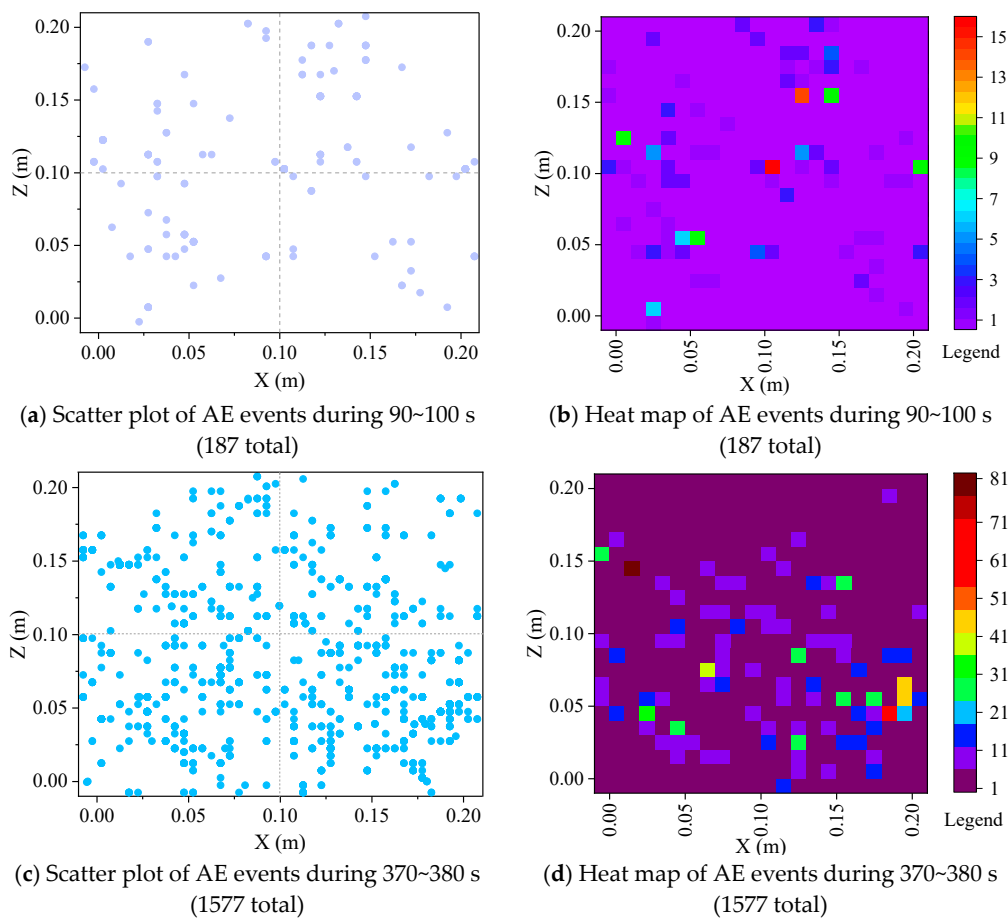


Figure 8. Cont.

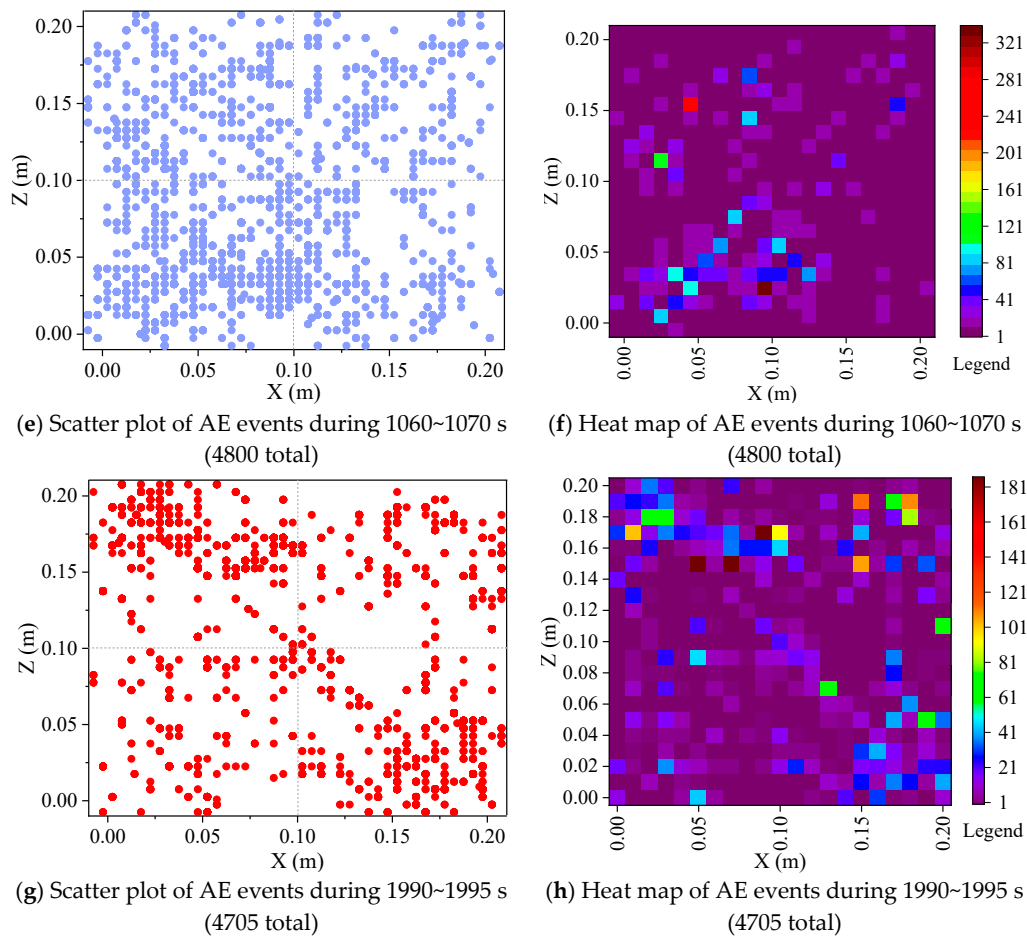


Figure 8. Scatter plot and heat map of AE event distribution during the typical periods.

Table 2. Number of AE event during the typical periods.

Time Period	Duration	Number of AE Events
90~100 s	10	187
370~380 s	10	1577
1060~1070 s	10	4800
1990~1995 s	5	4705

4. Discussion

Based on the above analysis in the Results chapter, the phased characteristics of energy during the uniaxial loading process of the sample, the waveform characteristics of AE events in different stages, and the distribution of the AE scatter plot and heat map in the typical stages were determined. The results show that during the later stage of high-energy AE events, the waveform display cannot accurately pick up the take-off point. The event distribution heat map obtained using the SSA is generally butterfly shaped in the later stage, which is consistent with previous theoretical research and numerical simulation results. This study focuses on the shape of the plastic zone around a hole when the sample fails in a wide range; therefore, the distribution characteristics of AE events in the period from 1990~1995 s should be deeply discussed.

The positioning results of AE events are three-dimensional coordinates; Figure 8 shows the XZ direction positioning in different periods, as it is necessary to analyze the number of positioning events in different Y ranges, and the results are shown in Figure 9. It can be seen from the results that the highest number of events occurred in the Y range of 0.03~0.04 m, which is 1016, followed by 438 in the Y range of 0.18~0.19 m. The number of AE events

on the two sides of the sample is greater, while the event number in the middle is relatively less. The vertical loading force of the sample is the same on the horizontal plane of the sample, but from the positioning results in the Y direction, the numbers of AE events in each range are relatively different, which may be related to the boundary conditions and the distribution or expansion of cracks in the sample.

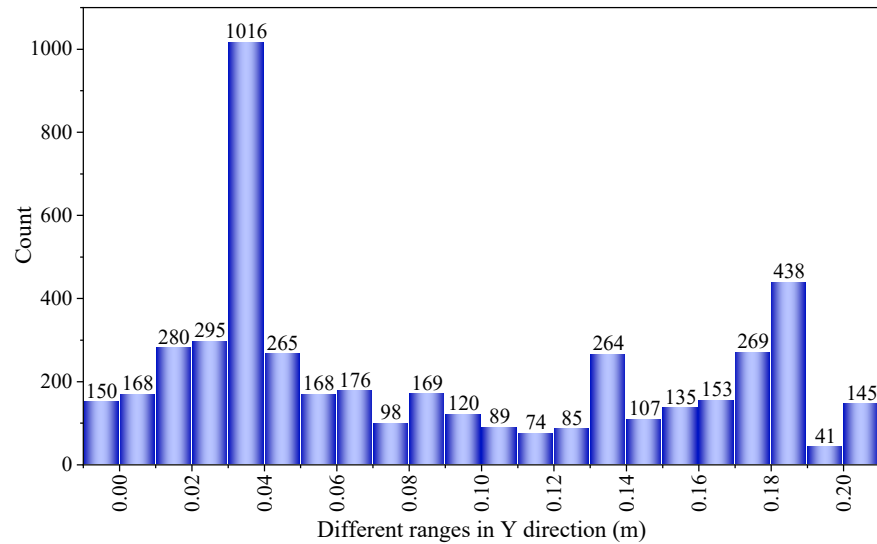
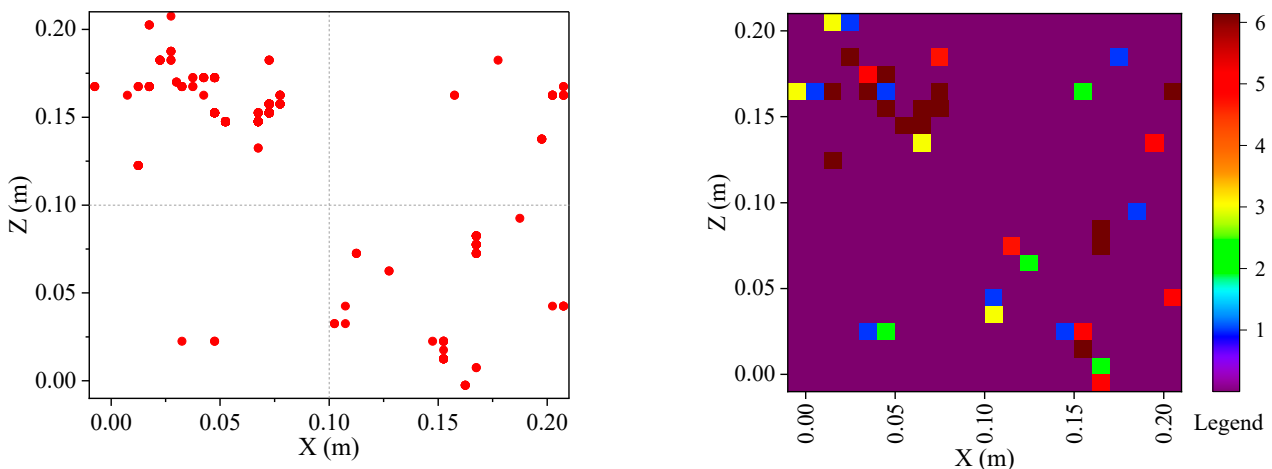


Figure 9. Histogram of AE event numbers occurring in different Y ranges.

In view of the high number (1016 total) of events within the range of $0.03\text{ m} < Y < 0.04\text{ m}$, a scatter plot and heat map are also presented in Figure 10. From the distribution of the scatter diagram, there are also some butterfly-shaped signs. Visually, the lower number of points displayed in the scatter plot is due to the coincidence of some events, and the heat map can better reflect the number of events in different areas, which also reflects that the events mainly occurred at four oblique angles (agglomeration in the butterfly leaf region). The number of events occurring in the range of $0.03\text{ m} < Y < 0.04\text{ m}$ accounts for $1016/4705 = 21.6\%$ of the total events, which indicates that the events do not occur uniformly in the sample but may also produce local agglomeration in a longitudinal region.



(a) Scatter plot of AE events with $0.03\text{ m} < Y < 0.04\text{ m}$ during 1990~1995 s (1016 total) (b) Heat map of AE events with $0.03\text{ m} < Y < 0.04\text{ m}$ during 1990~1995 s (1016 total)

Figure 10. Scatter plot and heat map of AE events with $0.03\text{ m} < Y < 0.04\text{ m}$ during 1990~1995 s (1016 total).

Previous theoretical research results [55] showed that the angle between the butterfly leaf and the coordinate axis was about 45 ± 5 degree. Therefore, in order to compare our results with this study, the events (occurring during 1990~1995 s) of the four quadrants in this experimental study were fitted as a straight line to see the specific angles, as shown in Figure 11. The number of events in the four quadrants is 2224, 1016, 1007, and 458, respectively, and the fitting angles are 46, 38, 40, and 41, respectively. Although there are some differences between the experimental results and the theoretical results, the gap is not large, and the shape of the butterfly plastic zone can also be verified from the butterfly leaf angles. In addition, it is worth noting that the number of events in the four quadrants varies greatly, which is a little different from the results of theoretical calculations and numerical simulations, and this fact may be mainly related to the heterogeneity of the sample and the application mode of external pressure.

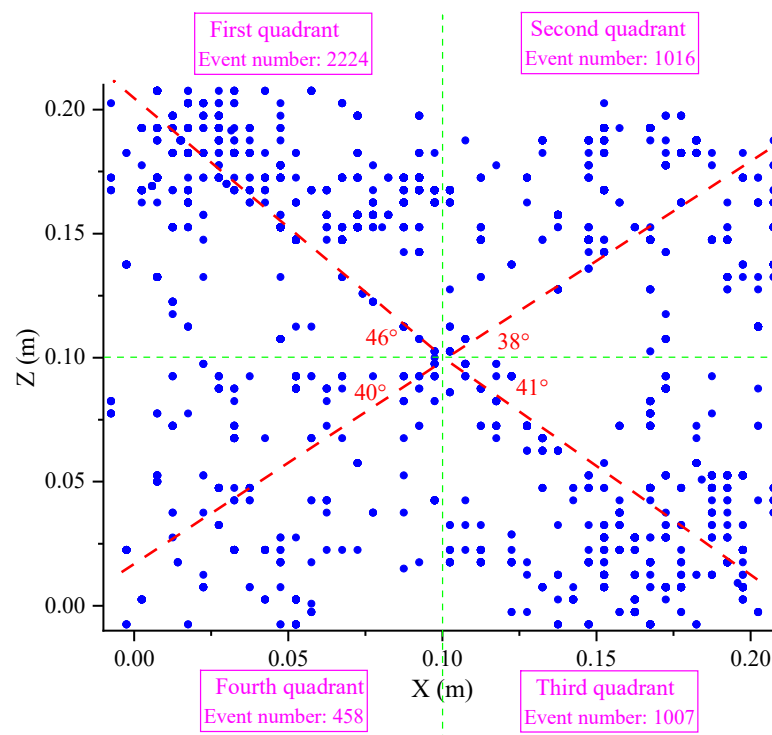


Figure 11. The fitted angles of the events (occurring during 1990~1995 s) in the four quadrants.

In order to more vividly and stereoscopically display the distribution characteristics of events during 1990~1995 s, a three-dimensional scatter plot and heat map are shown in Figure 12. The three-dimensional scatter plot in Figure 12a shows some butterfly morphological characteristics; relatively few events occur in the left lower butterfly leaf of the sample, and the numbers in the remaining three butterfly leaves are relatively high. It can be more clearly seen from the heat map in Figure 12b that the shape of the plastic zone formed in the sample is displayed as a three-dimensional butterfly. The results show that the number of events near the central hole of the sample is lower than that near the butterfly leaf. Figure 12b also figuratively indicates that the plastic zone basically shows a butterfly shape in different Y ranges, and the only difference may lay in the number of events distributed on each butterfly leaf. Among the four butterfly leaves, the greatest number of events occurred near the butterfly leaf in the upper left corner, which indicates that the heterogeneity of the actual butterfly leaf is a little different from theoretical research and numerical simulations, and this reason may also relate to the actual uneven properties of the sample.

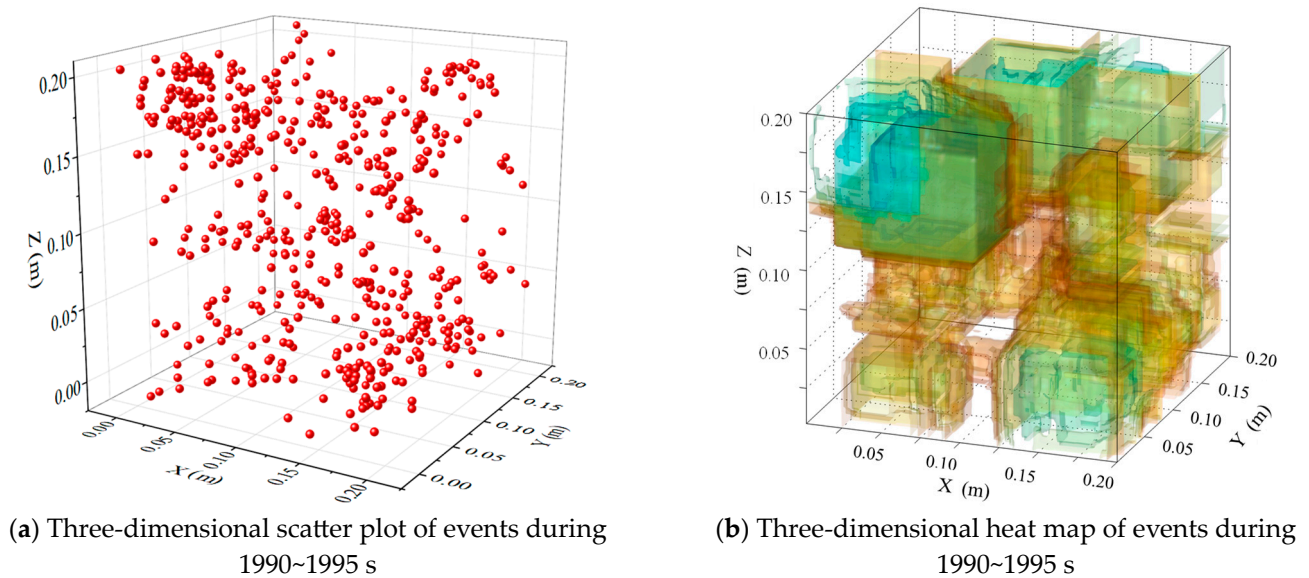


Figure 12. Three-dimensional scatter plot and heat map of events during 1990-1995 s.

In this study, the butterfly plastic zone shape of a rock sample with a central hole near failure under uniaxial loading was verified using experiments, which is of great significance to the study of rock failure. This research adopted relatively large samples, a relatively high sampling frequency, an appropriate algorithm, and the statistical results of big data. However, it has to be said that only the SSA was used for the event location due to the large amount of data, and there must be some errors in the location results. The errors were mainly from the rationality of the network, the value of wave velocity, the accuracy of the algorithm, etc. Moreover, more localization algorithms should be applied to improve the accuracy of localization and this could also be mutually verified. Compared with a previous study [56], the number of events used to locate the butterfly plastic zone was significantly increased to 4705, and the results of big data could inevitably reduce the degree of error. In future experimental research, transverse loading should apply to further verify the correctness of the butterfly plastic zone. The fact that the plastic zone in the early stage of rock failure in this study tended to be butterfly shaped preliminarily indicates the fractal law of rock failure. In the moment before rock failure, the distribution of AE events is more regular, which leads to large-scale collapse type failure.

5. Conclusions

In this study, a vibration signal acquisition system was used to collect AE events of a large sample under uniaxial compression. The results show that the take-off points were unclear near rock failure, and the location algorithm that depends on the take-off point was not able to work. Therefore, an SSA which depends on the luminance function was used to locate AE events. The shape of the plastic zone around the hole near the failure time was obtained in this experimental study; the morphological characteristics of the butterfly plastic zone were basically the same as the previous theoretical calculation and numerical simulation results, which verifies the correctness of butterfly failure theory at the laboratory scale. In addition, from the results shown in the discussion, the number difference of events in different quadrants indicates that the distribution of events in the four butterfly leaves is much higher than that in other locations, which is also consistent with previous findings. The experimental results reveal the shape of the plastic zone before rock failure, and more importantly, they provide a new idea for the mechanism and early warning method of rock failure, that is, taking the shape of the butterfly plastic zone as the mechanism of rock failure and applying it as a monitoring index of geotechnical disasters. Although it is difficult to monitor the shape of the plastic zone at the present stage, it is believed that

monitoring and early warning based on butterfly failure theory could be feasible with the development of monitoring technology.

Author Contributions: Conceptualization, W.Z.; methodology, J.M.; software, J.Y.; validation, W.Z.; formal analysis, W.Z.; investigation, J.R.; resources, C.L.; data curation, J.R.; writing—original draft preparation, W.Z.; writing—review and editing, J.M. All authors have read and agreed to the published version of the manuscript.

Funding: The authors gratefully acknowledge the financial support provided by the Qingdao Huanghai University Doctoral Research Fund Project (2022boshi02).

Data Availability Statement: The data presented in this study are available from the corresponding author upon request.

Conflicts of Interest: Jiajia Yu was employed by Zhejiang Qinhe Environmental Construction Co., Ltd.; Chen Li was employed by CCTEG Wuhan Engineering Company & Research Institute Co., Ltd. Other authors declare no conflicts of interest.

References

- Małkowski, P.; Juszyński, D. Roof fall hazard assessment with the use of artificial neural network. *Int. J. Rock Mech. Min. Sci.* **2021**, *143*, 104701. [[CrossRef](#)]
- Guo, W.-Y.; Zhao, T.-B.; Tan, Y.-L.; Yu, F.-H.; Hu, S.-C.; Yang, F.-Q. Progressive mitigation method of rock bursts under complicated geological conditions. *Int. J. Rock Mech. Min. Sci.* **2017**, *96*, 11–22. [[CrossRef](#)]
- Wang, G.-F.; Li, G.; Dou, L.-M.; Mu, Z.-L.; Gong, S.-Y.; Cai, W. Applicability of energy-absorbing support system for rockburst prevention in underground roadways. *Int. J. Rock Mech. Min. Sci.* **2020**, *132*, 104396. [[CrossRef](#)]
- Kong, Y.; Li, X.; Zhao, J. Quantifying the transition of impact mechanisms of geophysical flows against flexible barrier. *Eng. Geol.* **2021**, *289*, 106188. [[CrossRef](#)]
- Li, J.; Deng, S.; Wang, M.; Huang, H. Weak disturbance-triggered seismic events: An experimental and numerical investigation. *Bull. Eng. Geol. Environ.* **2018**, *78*, 2943–2955. [[CrossRef](#)]
- Chen, X.; Li, L.; Wang, L.; Qi, L. The current situation and prevention and control countermeasures for typical dynamic disasters in kilometer-deep mines in China. *Saf. Sci.* **2019**, *115*, 229–236. [[CrossRef](#)]
- Feng, X.-T.; Kong, R.; Yang, C.; Zhang, X.; Wang, Z.; Han, Q.; Wang, G. A Three-Dimensional Failure Criterion for Hard Rocks Under True Triaxial Compression. *Rock Mech. Rock Eng.* **2019**, *53*, 103–111. [[CrossRef](#)]
- Bukowska, M. Post-Peak Failure Modulus in Problems of Mining Geo-Mechanics. *J. Min. Sci.* **2013**, *49*, 731–740. [[CrossRef](#)]
- Liu, J.-P.; Wang, R.; Lei, G.; Si, Y.-T.; Xu, S.-D.; Li, Y.-H. Studies of stress and displacement distribution and the evolution law during rock failure process based on acoustic emission and microseismic monitoring. *Int. J. Rock Mech. Min. Sci.* **2020**, *132*, 104384. [[CrossRef](#)]
- Ranjith, P.G.; Zhao, J.; Ju, M.; De Silva, R.V.S.; Rathnaweera, T.D.; Bandara, A.K.M.S. Opportunities and Challenges in Deep Mining: A Brief Review. *Engineering* **2017**, *3*, 546–551. [[CrossRef](#)]
- Zhao, C.; Zhang, Z.; Lei, Q. Role of hydro-mechanical coupling in excavation-induced damage propagation, fracture deformation and microseismicity evolution in naturally fractured rocks. *Eng. Geol.* **2021**, *289*, 106169. [[CrossRef](#)]
- Voznesenskii, A.S.; Osipov, Y.V.; Ushakov, E.I.; Semyonov, Y.G.; Vasilevykh, V.V. Effect of weak inclusions on the fracture toughness of interfaces between various rocks. *Eng. Fail. Anal.* **2023**, *146*, 107140. [[CrossRef](#)]
- Voznesenskii, A.S.; Ushakov, E.I. Temperature dependence of internal mechanical losses of gypsum stone with complex composition and structure. *J. Alloys Compd.* **2022**, *906*, 164194. [[CrossRef](#)]
- Guo, X.; Zhao, Z.; Gao, X.; Wu, X.; Ma, N. Analytical solutions for characteristic radii of circular roadway surrounding rock plastic zone and their application. *Int. J. Min. Sci. Technol.* **2019**, *29*, 263–272. [[CrossRef](#)]
- Li, C.; Guo, X.; Lian, X.; Ma, N. Failure Analysis of a Pre-Excavation Double Equipment Withdrawal Channel and Its Control Techniques. *Energies* **2020**, *13*, 6368. [[CrossRef](#)]
- Zhang, W.; Ma, N.; Ma, J.; Li, C.; Ren, J.; Jiang, B. Mechanism of Rock Burst Revealed by Numerical Simulation and Energy Calculation. *Shock. Vib.* **2020**, *2020*, 8862849. [[CrossRef](#)]
- Zhao, Z. *Mechanism of Surrounding Rock Deformation and Failure and Control Method Research in Large Deformation Mining Roadway*; China University of Mining and Technology: Beijing, China, 2014.
- Zhao, Z.; Ma, N.; Liu, H.; Guo, X. A butterfly failure theory of rock mass around roadway and its application prospect. *J. China Univ. Min. Technol.* **2018**, *47*, 969–978.
- Guo, X.; Zhao, Z.; Gao, X.; Ma, Z.; Ma, N. The Criteria of Underground Rock Structure Failure and Its Implication on Rockburst in Roadway: A Numerical Method. *Shock. Vib.* **2019**, *2019*, 7509690. [[CrossRef](#)]
- Wu, X.; Liu, H.; Li, J.; Guo, X. Space-time Evolutionary Regularity of Plastic Zone and Stability Control in Repetitive Mining Roadway. *J. China Coal Soc.* **2020**, *2020*, 1–16.

21. Guo, X.; Guo, L.; Ma, N.; Zhao, Z. Applicability analysis of the roadway butterfly theory. *J. China Univ. Min. Technol.* **2020**, *49*, 646–653.
22. Guo, X.; Guo, L.; Li, C.; Ma, N. A quantitative assessment method of roadway rockburst risk based on the plastic zone shape coefficient. *J. China Univ. Min. Technol.* **2021**, *50*, 39–49.
23. Hao, Z. *Evolution Law of Plastic Zone and Burst Failure Mechanism of Gateway in Yima Coalfield*; China University of Mining and Technology: Beijing, China, 2018.
24. Liu, H.; Qiao, B.; Ma, N. Stability analysis and design of roadways in adjacent seams: A case study from Tashan coal mine in China. *Arab. J. Geosci.* **2020**, *13*, 308. [[CrossRef](#)]
25. Gao, X.; Ma, Z.; Shi, H.; Feng, J. Energy release induced rockbursts based on butterfly-shaped plastic zones in roadways of coal reservoirs. *PLoS ONE* **2021**, *16*, e0255044. [[CrossRef](#)] [[PubMed](#)]
26. Liu, H.; Guo, L.; Zhao, X.; Wang, P. Effect of Principal Stress Field on the Development of Plastic Zone ahead of the Gateroad. *Energies* **2020**, *13*, 4356. [[CrossRef](#)]
27. Ma, N.; Feng, J.; Lv, K.; Zhao, Z. Study on cause classification method and support countermeasures of roof falling in coal drift. *Coal Sci. Technol.* **2015**, *43*, 34–40.
28. Qiao, J.; Ma, N.; Ma, J.; Zhao, Z. Conjugate shear fracture-seismic composite model based on structural stability of dynamic system. *J. China Coal Soc.* **2019**, *44*, 1647–1653.
29. Ma, N.; Ji, M.; Zhiqiang, Z.; Xiaofei, G. Mechanical mechanism and evolution of X-shaped conjugate shear fractures-seism. *J. China Coal Soc.* **2019**, *44*, 1647–1653.
30. Shi, H.; Huang, P.; Ma, N.; Wang, Y. Evolution of regional tectonic system in the longmenshan mountains based on plastic dislocation theory of rocks. *Acta Geol. Sin.* **2020**, *94*, 3581–3589. [[CrossRef](#)]
31. Ma, N.; Zhao, X.; Zhao, Z.; Guo, X. Conjecture about mechanism of butterfly-shape coal and gas outburst in excavation roadway. *J. Min. Sci. Technol.* **2017**, *2*, 137–149.
32. Li, D.; Wang, E.; Kong, X.; Ali, M.; Wang, D. Mechanical behaviors and acoustic emission fractal characteristics of coal specimens with a pre-existing flaw of various inclinations under uniaxial compression. *Int. J. Rock Mech. Min. Sci.* **2019**, *116*, 38–51. [[CrossRef](#)]
33. Zhang, Z.; Wang, E.; Li, N. Fractal characteristics of acoustic emission events based on single-link cluster method during uniaxial loading of rock. *Chaos Solitons Fractals* **2017**, *104*, 298–306. [[CrossRef](#)]
34. Lin, P.; Wei, P.; Wang, C.; Kang, S.; Wang, X. Effect of rock mechanical properties on electromagnetic radiation mechanism of rock fracturing. *J. Rock Mech. Geotech. Eng.* **2021**, *13*, 798–810. [[CrossRef](#)]
35. Su, G.; Shi, Y.; Feng, X.; Jiang, J.; Zhang, J.; Jiang, Q. True-Triaxial Experimental Study of the Evolutionary Features of the Acoustic Emissions and Sounds of Rockburst Processes. *Rock Mech. Rock Eng.* **2017**, *51*, 375–389. [[CrossRef](#)]
36. Voznesenskii, A.S.; Krasilov, M.N.; Kutkin, Y.O.; Tavostin, M.N.; Osipov, Y.V. Features of interrelations between acoustic quality factor and strength of rock salt during fatigue cyclic loadings. *Int. J. Fatigue* **2017**, *97*, 70–78. [[CrossRef](#)]
37. Voznesenskii, A.S.; Kutkin, Y.O.; Krasilov, M.N.; Komissarov, A.A. The influence of the stress state type and scale factor on the relationship between the acoustic quality factor and the residual strength of gypsum rocks in fatigue tests. *Int. J. Fatigue* **2016**, *84*, 53–58. [[CrossRef](#)]
38. Voznesenskii, A.S.; Kutkin, Y.O.; Krasilov, M.N.; Komissarov, A.A. Predicting fatigue strength of rocks by its interrelation with the acoustic quality factor. *Int. J. Fatigue* **2015**, *77*, 194–198. [[CrossRef](#)]
39. Ren, F.; Zhu, C.; He, M. Moment Tensor Analysis of Acoustic Emissions for Cracking Mechanisms During Schist Strain Burst. *Rock Mech. Rock Eng.* **2019**, *53*, 153–170. [[CrossRef](#)]
40. Zhang, W.; Li, C.; Huo, T.; Qu, X.; Xin, C. Vibration events in underground heading face and useful index for rock burst monitoring. *Measurement* **2021**, *180*, 109501. [[CrossRef](#)]
41. Zhang, W.; Ma, N.; Ren, J.; Li, C. Peak particle velocity of vibration events in underground coal mine and their caused stress increment. *Measurement* **2021**, *169*, 108520. [[CrossRef](#)]
42. Lian, X.; Zhang, W.; Li, C.; Guo, X. Application of discrete data extreme value distribution in the analysis of mine pressure rule. *Arab. J. Geosci.* **2021**, *14*, 2011. [[CrossRef](#)]
43. Carpinteri, A.; Lacidogna, G.; Accornero, F.; Mpalaskas, A.C.; Matikas, T.E.; Aggelis, D.G. Influence of damage in the acoustic emission parameters. *Cem. Concr. Compos.* **2013**, *44*, 9–16. [[CrossRef](#)]
44. Jiang, L.; Kong, P.; Zhang, P.; Shu, J.; Wang, Q.; Chen, L.; Wu, Q. Dynamic Analysis of the Rock Burst Potential of a Longwall Panel Intersecting with a Fault. *Rock Mech. Rock Eng.* **2019**, *53*, 1737–1754. [[CrossRef](#)]
45. Zhang, R.; Dai, F.; Gao, M.Z.; Xu, N.W.; Zhang, C.P. Fractal analysis of acoustic emission during uniaxial and triaxial loading of rock. *Int. J. Rock Mech. Min. Sci.* **2015**, *79*, 241–249. [[CrossRef](#)]
46. Zhang, W.; Lian, X.; Wu, Z. A multi-channel verification index to improve distinguish accuracy of target signals in rock burst monitoring of heading face. *Measurement* **2021**, *189*, 110483. [[CrossRef](#)]
47. Li, Q.-Y.; Dong, L.-J.; Li, X.-B.; Yin, Z.-Q.; Liu, X.-L. Effects of sonic speed on location accuracy of acoustic emission source in rocks. *Trans. Nonferrous Met. Soc. China* **2011**, *21*, 2719–2726. [[CrossRef](#)]
48. Wang, C.; Si, G.; Zhang, C.; Cao, A.; Canbulat, I. Location error based seismic cluster analysis and its application to burst damage assessment in underground coal mines. *Int. J. Rock Mech. Min. Sci.* **2021**, *143*, 104784. [[CrossRef](#)]

49. Pu, Y.; Apel, D.B.; Hall, R. Using machine learning approach for microseismic events recognition in underground excavations: Comparison of ten frequently-used models. *Eng. Geol.* **2020**, *268*, 105519. [[CrossRef](#)]
50. Dong, L.; Sun, D.; Li, X.; Du, K. Theoretical and Experimental Studies of Localization Methodology for AE and Microseismic Sources Without Pre-Measured Wave Velocity in Mines. *IEEE Access* **2017**, *5*, 16818–16828. [[CrossRef](#)]
51. Kao, H.; Shan, S.-J. The Source-Scanning Algorithm: Mapping the distribution of seismic sources in time and space. *Geophys. J. Int.* **2004**, *157*, 589–594. [[CrossRef](#)]
52. Zahradník, J.; Janský, J.; Plicka, V. Analysis of the source scanning algorithm with a new P-wave picker. *J. Seismol.* **2014**, *19*, 423–441. [[CrossRef](#)]
53. Kao, H.; Shan, S.-J. Rapid identification of earthquake rupture plane using Source-Scanning Algorithm. *Geophys. J. Int.* **2007**, *168*, 1011–1020. [[CrossRef](#)]
54. Kong, X.; Wang, E.; He, X.; Li, D.; Liu, Q. Time-varying multifractal of acoustic emission about coal samples subjected to uniaxial compression. *Chaos Solitons Fractals* **2017**, *103*, 571–577. [[CrossRef](#)]
55. Guo, X. *Criterion of Plastic Zone Shapes of Roadway Surrounding Rock and Its Application*; China University of Mining and Technology: Beijing, China, 2019.
56. Aker, E.; Kühn, D.; Vavryčuk, V.; Soldal, M.; Oye, V. Experimental investigation of acoustic emissions and their moment tensors in rock during failure. *Int. J. Rock Mech. Min. Sci.* **2014**, *70*, 286–295. [[CrossRef](#)]

Disclaimer/Publisher’s Note: The statements, opinions and data contained in all publications are solely those of the individual author(s) and contributor(s) and not of MDPI and/or the editor(s). MDPI and/or the editor(s) disclaim responsibility for any injury to people or property resulting from any ideas, methods, instructions or products referred to in the content.